Journal of Nondestructive Evaluation (2022) 41:41
https://doi.org/10.1007/s10921-022-00870-5

Experimental Procedure to Assess Depth and Size of Defects with Pulsed Thermography

Ester D'Accardi[1] · Davide Palumbo[1] · Umberto Galietti[1]

Received: 20 January 2021 / Accepted: 25 March 2022 / Published online: 16 May 2022

Abstract
Subsurface defects can be detected by the pulsed thermography (PT) technique analysing the raw thermal data with the application of different post-processing algorithms. In this regard, different methods, based on one-dimensional models, are used in the literature to estimate the depth and size of defects. Two of the most established methods are the thermal signal reconstruction (TSR) and the pulsed phase thermography (PPT) algorithms. These latter require a careful set up of the testing parameters such as the frame rate, the truncation window size, and the energy density to obtain an accurate estimation of both depths and sizes of defects. Even if some works have already investigated the issue of defect characterization, there are few works in which the correct procedures to obtain both the size and depth were deeply explained, above all for real components with real defects. The aim of this work is to propose a new empirical procedure to obtain depth and size estimation of the defects using the pulsed thermography technique and in particular the principal component thermography (PCT) algorithm. The proposed procedure is based on the experimental observation that exists a linear correlation between the defect contrasts and the relative aspect ratios. In this way, by means of a master specimen, a calibration curve can be obtained considering a suitable truncation window of the analysed data. Then, the size and depth of defects have been retrieved imposing threshold criteria. The procedure is quite general, and it can be also tested with other algorithms. Different experimental tests have been carried out on two materials, aluminium and glass fiber reinforced polymer (GFRP) and then the procedure has been applied and validated both on simulated (flat bottom holes) and real defects.

Keywords Pulsed thermography · Principal component thermography (PCT) · Defect characterization · NDT procedure · Quantitative assessment

1 Introduction

The non-destructive tests (NDT) have a crucial role in detecting and quantifying defects that could compromise the structural integrity of components and structures. In this regard, it is very important to characterize defects with good accuracy for evaluating the residual strength of components.

In the last years, many stimulated thermographic techniques have been investigated with the aim to obtain fast information of the defect size and depth. These techniques are based on the generation of a heat flow induced into the material by means of external excitations, with a transmission or reflection setup [1].

✉ Ester D'Accardi
ester.daccardi@poliba.it

[1] Department of Mechanics, Mathematics and Management, Polytechnic University of Bari, Via Orabona 4, 70125 Bari, Italy

The pulsed thermography technique (PT) [1], as well as its variations such as long pulsed thermography, is used in many applications to detect defects in several materials, from metals to composites, because it requires a simple setup and allows fast defect detection. Generally, the application of post-processing algorithms is necessary because raw thermal data are not suitable for correct thermographic analysis, especially if quantitative information in terms of depth and size [2] must be retrieved. Furthermore, it is well-known that the additional application of different algorithms improves the signal-to-noise-ratio, which allows for detection of smallest defects. In this regard, in the last years, several algorithms have been developed to improve the signal contrast and to develop quantitative thermographic procedures, such as the thermal signal reconstruction (TSR) [3–5], the pulsed phase thermography (PPT) [6–8] and the principal component thermography (PCT) [9]. These well-established methods are based on the one-dimensional model of the heat conduction

equation from which the information about the defect depth can be roughly estimated [10–13].

Basically, the TSR algorithm analyses the measured thermographic data in the time domain, investigating the first and second derivative of the thermal sequences [2–4, 5], after its polynomial fitting in a double logarithmic scale.

The PPT algorithm [6–8], evaluates the cooling thermal behaviour in the frequency domain, by means of the Fast Fourier Transformation (FFT) of raw data. Both techniques require the knowledge of the thermophysical properties of the material for obtaining the estimation of the defect depth. However, these methods present some weak points in defect depth estimation, as already demonstrated in previous works [2].

Firstly, it has to be remarked that the accuracy of depth estimation depends on the frame rate adopted for sampling the physical process (thermal cooling curve). Indeed, for high diffusivity materials, such as the aluminium alloys, a high error in depth estimation can be obtained if high frame rates (> 500 Hz) are not used. It follows that an infrared detector with high performances and then with a high cost must be used [14–17, 18], to ensure the desired precision and accuracy. Another limit of the methods based on the 1D model is related to the 3D thermal behaviour effects on the thermal signal due to the finite defect dimension. As demonstrated in different works [2, 10–15, 19–21], the accuracy in the assessment of the defect depth is affected by the defect dimension. In this regard, Almond et al. [22, 23], presented a simple analytical expression to model the dependence of the signal contrast on defect aspect ratio. This model shows that a more accurate depth estimation can be obtained if the defect aspect ratio is considered. Finally, 1D models consider plane semi-infinite defects neglecting the effect of the shape of the defect that can further affect the size and depth estimation [24–26]. In fact, it is mandatory to underline that the signal contrast depends on the defect size, depth, and shape, as already demonstrated in previous works [2, 10–15, 19–21].

Another important point to remark is that in the literature there are many works about defects detection, but very few works that describe the complete procedure for obtaining quantitative results from a pulsed thermographic test. Indeed, the accuracy of quantitative results depends not only on the adopted algorithm, but also on many other parameters such as experimental set-up, pre-processing of the thermal data, temporal length of the acquired sequence, etc.

The PCT [9] consists of the application of the Singular Value Decomposition (SVD) to the thermal raw data, with the advantages to obtain a rapid feature extraction, data compression, and noise reduction. Compared with the original raw data, the obtained PCT feature maps present a significant improvement of data in term of the signal to noise ratio [14, 27–30]. Usually, the PCT algorithm is used to retrieve the in-plane defect dimensions while there are few works that exploit the temporal data information. In the work of Raijic [9], the processed data have been also used for estimating the depth of simulated defects of a composite laminate.

In this work, a new empirical procedure for the quantitative analysis of thermographic data is proposed, with the aim to overcome the limitations of traditional 1D formulations and finding a common approach valid for different materials and set-ups. The proposed approach has been applied to thermographic data processed by means of the well-known Principal Component Thermography (PCT) algorithm.

Starting from the previous considerations, the proposed approach aims to obtain the estimation of both the size and depth of defects by using only the spatial information of the signal contrast deriving from the PCT processing, for two different materials, aluminium alloy (high diffusivity) and glass fiber composite material—GFRP (low diffusivity) and two different experimental setups. Two fundamental aspects were taken into account, the use of a master specimen with imposed known defects (a common approach to other NDT techniques) and the influence of the defect shape by considering the "equivalent defect dimension", defined as the characteristic dimension of the defect directly related to the signal contrast.

The proposed procedure has been tested on a real component, a piece of GFRP wind blade with real volumetric defects inside (air gaps). Moreover, the depth estimation with the proposed procedure on the GFRP component have been compared to those obtained with the well-established ultrasonic testing (A-scan) [31–34], providing very promising results.

2 Theory

The correct application of a post processing algorithm to analyse the raw thermal data is almost always necessary, for improving the quality of data in term of the signal-to-noise-ratio. In this context, the PCT is one of the most used algorithms, both for a short or long pulse, as demonstrated in many works [1, 9, 14, 22, 23, 27–30, 35–38]. The PCT is typically used to reduce the dimension of acquired thermal signals by projecting the original data set onto a system of orthogonal components [9]. The thermal raw data are presented as a 3D matrix, with dimensions indicated as 'i, j, k' (i index along the rows, j index along the columns and k index along the frames). To apply this algorithm, the background subtraction is initially performed to obtain the 3D matrix related to the delta temperature. Follows a reshape operation to convert the 3D matrix in a 2D (indicated with X), in a such a way that time variations will occur column-wise, while spatial variations will occur row-wise. This 2D matrix is then normalized, following the well-known operations described in [9], and here summarized:

$$\bar{X}\,(i * j,\, k) = \frac{X(i * j,\, k) - \mu}{\sigma} \tag{1}$$

where μ and σ are, respectively, the mean and the standard deviation values related to the rearranged 2D matrix X, and the symbol '*' represents the scalar product [9]. Follows the operation of the singular value decomposition (SVD), as reported below:

$$\bar{X}\,(i * j,\, k) = USV^T \tag{2}$$

The resulting U matrix that provides spatial information can be reconverted into a 3D sequence. In particular, in the SVD process, the matrix U consists of orthogonal functions representing the spatial variations of the thermal data set. Each column of U provides the coordinates of thermal signals in the space of principal components. The matrix S is a diagonal matrix with singular values on its diagonal that are arranged in a descending order. These singular values in S are the nonzero square root of the eigenvalue X^TX for the corresponding eigenvectors in the matrix V. The columns of matrix U are known as empirical orthogonal functions (EOF); as known, the first EOFs (5–6) represent nearly 80–90% of the variation of the measured thermal data associated with the spatial variation of the material defect, leaving the noise inside the successive U matrices.

In this work, the algorithm has been used as suggested in the literature, proposing for the first time a quantitative approach, linked to the depth and size of the defect by simply using the matrix of principal components U (spatial variations of the thermal data), and not the V matrix (where the principal component vectors are arranged row-wise) as rarely suggested in previous publications [9].

The procedure is based on the signal contrast and related quantitative criteria to define the defect detectability and its quantification. For this reason, the definition of the signal contrast and the normalized contrast is here reported, hereinafter indicated as Signal Background Contrast (SBC):

$$SBC = \frac{MS_D - MS_s}{SD_s} = \frac{Contrast_{EOFn}}{SD_s} = \frac{C_{EOFn}}{SD_s} \tag{3}$$

where MS_D is the signal due to the defect, MS_s is the mean value of the undamaged area (for simplicity indicated with the subscript s -sound and taken just near the defect, in an area sufficiently distant to not be affected by the defect itself), SD_U is the standard deviation of the undamaged area, C_{EOFn} is the contrast of the chosen *n-EOF*. To assess the MS_D value in correspondence of the signal peak of each defect (for defects such as flat bottom holes it is usually the central area, but for real defects it can be a different area), the average value of a 3 × 3 pixel array has been considered, while, to assess MS_U and SD_U values, the undamaged area has been considered [14].

3 Methods: Main Steps of the Proposed Procedure

The basic steps of the calibration procedure concern the analysis of a sample/master specimen with simulated known defects. This specimen must be manufactured according to the following steps:

i. Made of the same material of the component to analyse;
ii. The simulated defects must be representative of the real defects to detect in terms of typology and aspect ratio;
iii. An adequate number of defects must be simulated to have a wide range representative data (aspect ratio *D/d*).

The main steps of the proposed procedure are:

(a) Setting set-up and testing parameters;
(b) Acquiring thermal data (thermal sequence);
(c) Exporting the thermal sequence and pre-processing (delta temperature evaluation ΔT);
(d) Processing the entire sequence with the PCT algorithm and extracting the principal components (the first 6 EOF); are usually more than sufficient
(e) Calculating the SBC and the contrast for each detected defect. An undamaged area must be defined as reference (typically, an indication is considered as a defect only if there is a set of nearby pixels equal to or bigger than 9 [14]);
(f) Choosing a suitable threshold value Th_v on the obtained SBC, for a generic defect, to define the defect detectability $SBC > Th_v$ [14]; in this work a value equal to 2, usually used for non-destructive testing application, has been used;
(g) Choosing the EOF that provides the maximum number of defects;
(h) Re-processing the thermal sequence frame by frame (changing the truncation window size) with the PCT algorithm and extracting the chosen principal component (for example 2nd one)—Fig. 1;

(i) Evaluating the linear correlation between the SBC and D/d (R^2 = Pearson's coefficient), or equivalently the relation contrast—D/d, for each extracted map, corresponding to a suitable truncation window size;
(j) Identifying the map with the maximum R^2 value ('$EOF_n - R^2_{max}$') and assessing the linear regression coefficients (calibration curve)—Fig. 2;

(k) Choosing a set of different threshold values with the aim to separate the contribution of the thermal signal related

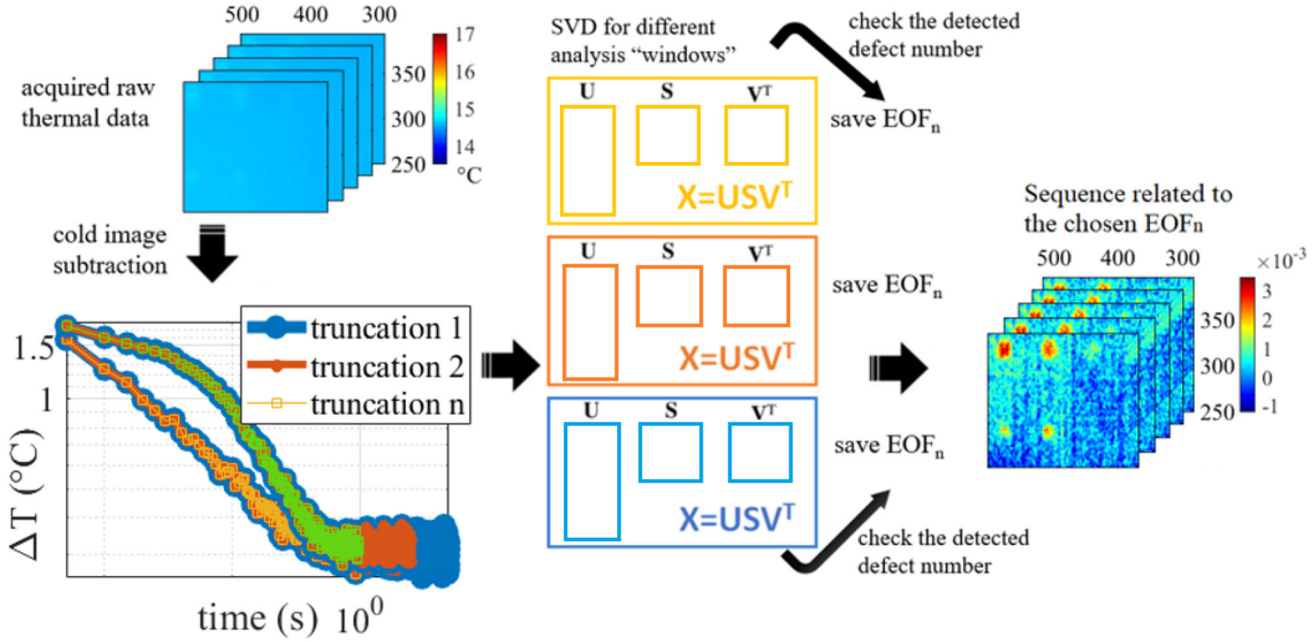

Fig. 1 Processing data analysis for the raw thermal data to obtain the sequence related to the chosen EOFn for the later analysis frame by frame (steps from a to h)

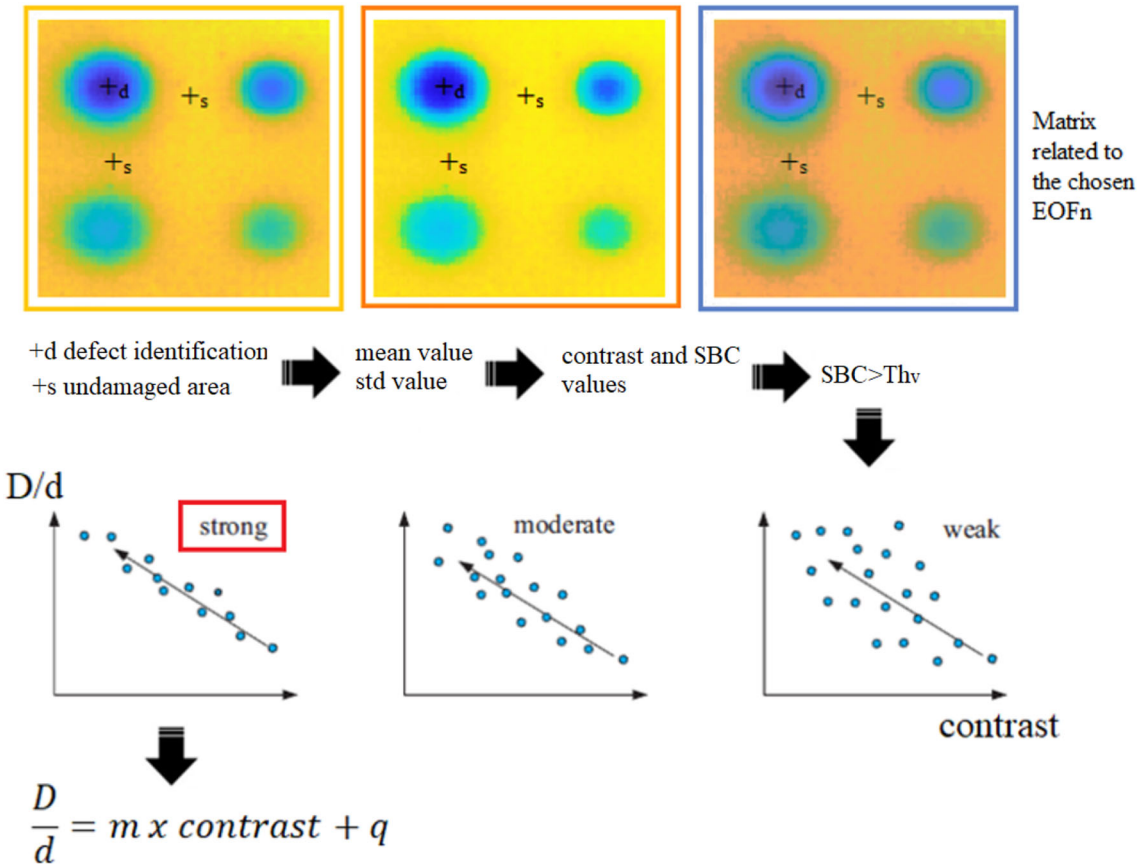

Fig. 2 Obtaining the calibration curve D/d-contrast (steps i and j)

to the defect depth d and the defect size D, considering only the selected map; the generic pixel (x, y) with the signal S_{EOF} is identified as a defect if one of the inequalities in Eq. 4 occurs:

$$\begin{cases} S_{EOF}(x,\,y) > MS_S + |MS_D - MS_S| Th_{D/d} & if\ MS_D - MS_S > 0 \\ S_{EOF}(x,\,y) < MS_S - |MS_D - MS_S| Th_{D/d} & if\ MS_D - MS_S < 0 \end{cases} \tag{4}$$

and then assigning to this pixel a value equal to 1 and 0, respectively (hit/miss data) based on the obtained result then assigning it a value equal to 1 and 0, respectively (hit/miss data);

(l) Calculating the error committed in quantitative estimation for each threshold value by knowing the nominal dimensions of the imposed defects;
(m) Defining for a suitable D/d range, the threshold value that minimizes the errors in the depth and size estimation, to create a set of curves 'D/d-threshold value'—N.B. $Th_{D/d}$ is different from Th_v; both are associated with the contrast, but Th_v discerns the defect detectability whilst $Th_{D/d}$ is related with the defect aspect ratio for quantifying the defect;
(n) Repeating all the previous steps, starting from the acquisition, at least 3 times, if possible, to obtain a more robust model. For this step, it is possible, and recommendable from a computational point of view, skip the steps *e, f, g* and *h* and analyse directly the window indicated as better from the first replication. It is worth to underline that in both Figs. 2 and 3 the linear correlation 'D/d-contrast' is represented by means of a line with a negative slope as the signal contrast has a negative sign—Fig. 3.

Here, a real case study is considered to try this procedure, following exactly all the steps explained here, and led to good results in comparison with ultrasound for 3 different real defects, air gaps, typical of GFRP materials.

4 Material and Experimental Set-Up

In this section, the set-ups, materials, specimens, and components used for obtaining and demonstrating the effectiveness of the proposed procedure will be described. In particular, two different materials in terms of thermophysical properties have been investigated and a real component with real defects has been used for demonstrating the feasibility of the proposed procedure.

4.1 High Diffusivity Material: The Sase of the Aluminium Material Investigation

In Fig. 4a is shown the aluminium specimen that presents several flat bottom holes of different diameters and depths. The defect nominal sizes and depths are reported in Fig. 4b.

The aspect ratios (*D/d* values) obtained by simulating these defects are different and cover a wide range from 1 to 20.

The adopted experimental set-up is shown in Fig. 5. The thermographic sequences have been acquired using the IR cooled camera FLIR X6540 SC with the thermal sensitivity (NETD) < 25 mK and a full-frame window of 640 × 512 pixels. Two flash lamps with a total energy of 3000 J and a pulse duration of 5 ms have been positioned very close to the specimen (10 cm) and at the same side of the IR camera. This latter has been placed at about 1 m from the specimen, in order to obtain a geometrical resolution of 0.25 mm/pixel. To reach a frame rate of 200 Hz, the frame window of the IR camera has been reduced to 464 × 328 pixels. In this way, two different tests have been carried out to apply the proposed procedure. The first one has been used for obtaining the calibration curve and it has involved all the defects within the blue window in Fig. 4, while the second one (red window) has been used for the demonstration. In particular, the demonstration has also interested the defects within the green window that have not been used for the calibration phase.

For each test, 3 replications have been performed leaving the set up unchanged.

4.2 Low Diffusivity Material: The Case of the GFRP Material Investigation

A GFRP specimen (total thickness about 16 mm), obtained through the vacuum infusion resin process, with different simulated defects (flat bottom holes) has been used to carry out the experimental investigation related to the composite material. An epoxy-type (i.e. EC 157 by ELANTAS, West Bengal, India) resin has been taken into account, reinforced with a double layer of quadriaxial glass fibre of the type 0°/45°/90°/45° (Fig. 6). Dimensions and depth of defects are reported in Fig. 6, for a range of *D/d* between 1 and 35 approximately. The part of the specimen used for these thermographic tests is highlighted in a red window.

The proposed procedure has been validated in this case on a real component made of the same material (description reported in a separate paragraph). The thermographic sequences have been acquired with the Flir A655sc IR cam-

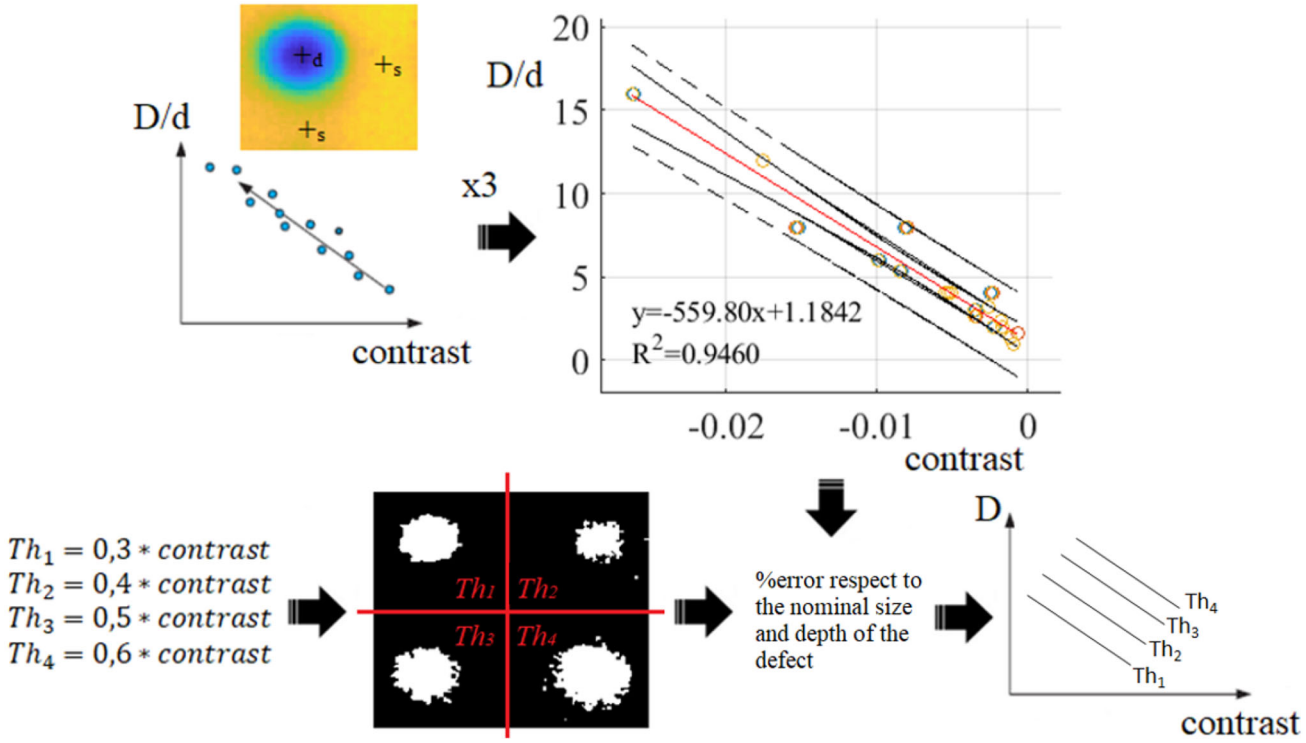

Fig. 3 Definition of the family of curves 'D/d-$Th_{D/d}$', with the aim to separate the contribution of the thermal signal related to the defect depth d and the defect size D (steps from k to n)

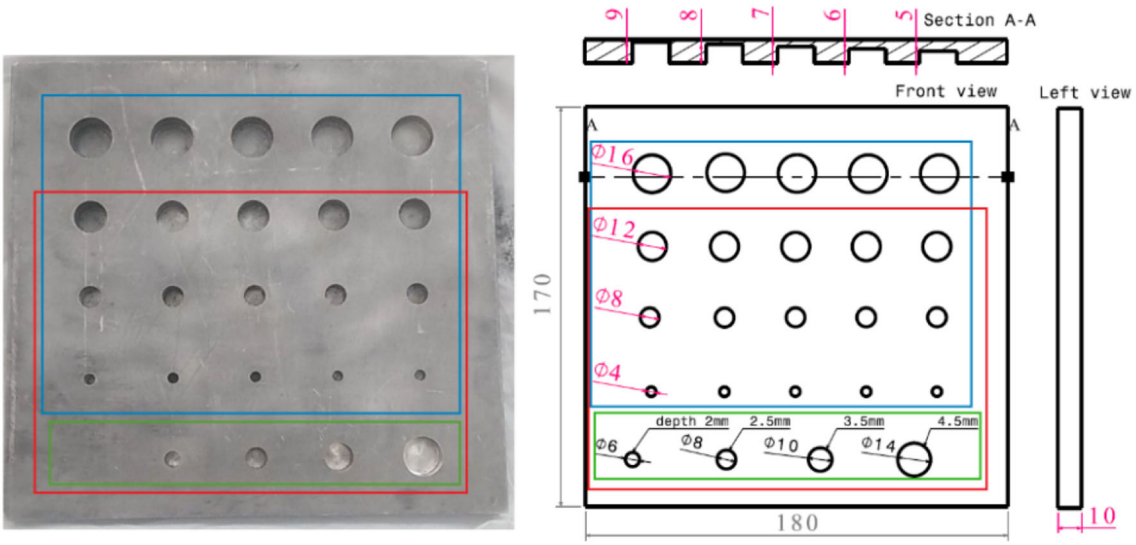

(a) **(b)**

Fig. 4 (a) Aluminium specimen with different flat bottom holes, with aspect ratios D/d from 1 to 20, and (b) the relative technical drawing with dimensions, depths and relative positions; blue window-part of the sample used for the calibration procedure, red window-part of the sample used for the demonstration remarking in green the defects created exclusively for this purpose (Color figure online)

Fig. 5 The used set-up for the thermographic pulsed tests performed on the aluminium specimen

era with a micro bolometric sensor of 640 × 512 pixels and NETD < 30 mK. The experimental set up is shown in Fig. 7 and the main distances are here resumed lamps angle: $\beta = 40°$, distance camera-sample 140 cm, distance lamps-sample 240 cm. In this way, a spatial resolution of 0.68 mm/pixel has been reached. Two halogen lamps of 1000 W have been used. A pulse duration of 220 s has been adopted with a frame rate of 1 Hz, for a total test duration of 1500 s. It is worth emphasizing again that for investigating thick components made of low-thermal diffusivity materials, the more suitable approach is to consider the long pulse technique in which high deposed energies are obtained increasing the pulse duration.

The ultrasonic technique (UT) has been used to compare and validate the achieved results in the investigation of the real GFRP component, and in particular to evaluate the defect depth. The EPOCH 600 Ultrasonic Flaw Detector with a probe of 1 MHz and a dimension of 0.5 inches has been used for ultrasonic measurements. To set the ultrasonic parameters such as the sound velocity, filters, and the gain, the upper part of the GFRP sample with calibrated steps has been used (Fig. 6).

5 Results and Discussion

In this session, the obtained results and the related discussion will be shown and summarized for both the aluminium material and the GFRP, considering both the analyses of the specimens with the imposed defects using for the calibration procedure and those related to validation and therefore to the component with real defects.

5.1 Results Related to the Aluminium Specimen

5.1.1 Applying the Calibration Procedure to Investigate the Aluminium Specimen

In Fig. 8 are summarized the obtained results, considering the part of the specimen used for the calibration (Fig. 4, blue box)

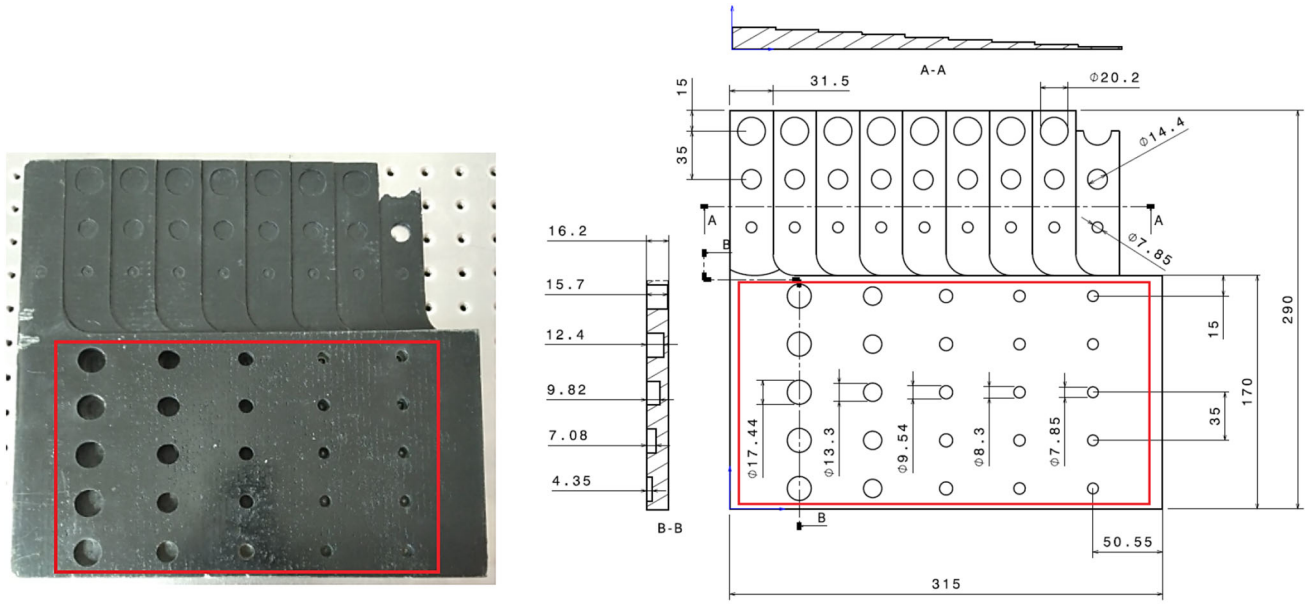

Fig. 6 **a** GFRP specimen with different flat bottom holes, with aspect ratios D/d from 1 to 35 and **b** the relative technical drawing with dimensions, depths and relative positions

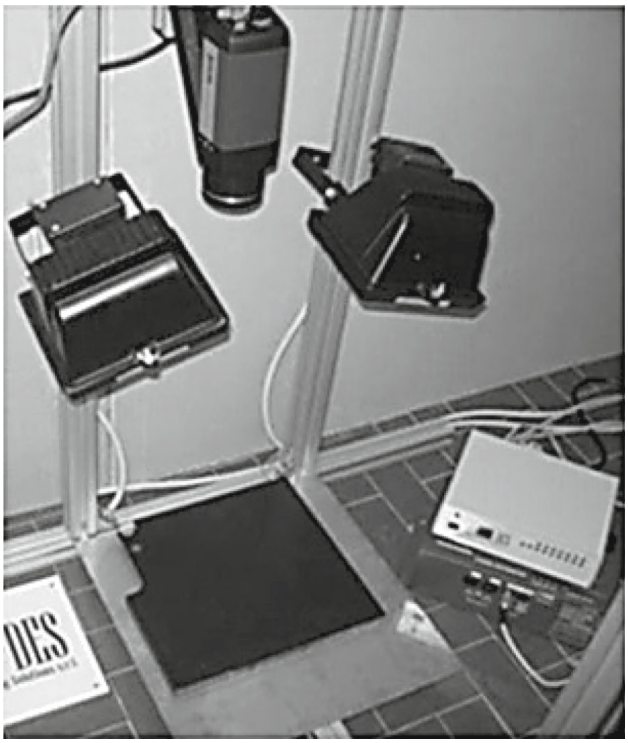

Fig. 7 The used set-up for the thermographic pulsed tests performed on the GFRP specimens [35]

and analysing the acquired thermal sequence for different truncation window sizes (scheme in Fig. 1).

Figure 8a shows, as an example, the typical thermal profiles that have been obtained in correspondence of the defect and the related undamaged area, indicated in Fig. 8c (diameter 12 mm, depth 2 mm), highlighting with 3 different colours the three different truncation windows. Figure 9c shows that the second component (EOF_2) provides the maximum number of defects, while the trend of the 2nd principal component (EOF_2) over time is shown in Fig. 8b, considering the same defect and the related undamaged area.

The next step of the procedure consists in identifying the truncation window for which both the maximum linear empirical correlation and a significant number of defects are detected. In this regard, Fig. 10 shows a similar result already shown in [14], in which the signal contrast related to the second principal component is linearly related to the aspect ratio, defect by defect, and for different truncation windows (reported as a number of frames); the defects with the signal contrast below to two times the undamaged area standard deviation have not been considered ($SBC > Th_v = 2$).

For each truncation window (frame by frame analysis), the square of the correlation coefficient R^2 has been assessed by means of the linear regression of aspect ratios on signal contrasts. In this regard, Fig. 11 shows the graph in which are present both the index R^2 and the number of detected defects, related to the first test replication. This graph allows for detecting the truncation window for which the maximum linear correlation is obtained (around 2 s). It is important to notice that the maximum values of R^2 and detected defects do not always occur for the same truncation window (as this graph clearly shows). In this regard, high R^2 values allow for obtaining a high correlation between the signal contrast and defect aspect ratio and then low systematic error in estimating the aspect ratios. On the contrary, in some cases, the operator could prefer to detect the maximum number of defects admitting a significant systematic error in defect estimation. In this case, the window related to 1.91 s has been chosen for the analysis (exact passage from 15 to 16 defects with the $SBC > 2$).

In Fig. 12a the EOF_2 map analysing 1.91 s is shown, in the case of the first test repetition, while in Fig. 12b the obtained calibration curve is reported, considering all the repetitions (indicated with three different colours). Moreover, in the same Fig. 12b are indicated also the confidence and prediction bounds adopting a confidence level of 95% [39, 40]. Considering homogeneous heating (the specimens have a regular geometry and size), it has been possible to adopt a unique undamaged area for all the defects in evaluating the *SBC* and in particular the mean and the undamaged area standard deviation for each defect (cross symbols in Fig. 12a).

The equation of the obtained calibration curve is reported in Eq. 5:

$$D/d = -636.32 x C_{EOF_2} + 1.20 \quad R^2 = 0.99 \tag{5}$$

the next step consist of determining the correct threshold value to separate the size and depth contribution. It is known that the contrast of a defect depends both on size and depth, and then only a *Th* value cannot be used to obtain the defect size of a wide range of defects.

As shown in Table 1, in this case, different threshold values must be used to assess the *D* value for each defect, specifying the percentage error (Eqs. 6, 7 and 8) with respect to the nominal dimensions (in this case, for flat bottom hole, the 2D plane dimension coincides with the nominal diameter) and with the sign information (defect underestimation or overestimation).

Table 1 summarizes the errors obtained in evaluating the diameter and the depth.

For two different ranges of *D/d*, here identified as suitable for the analysis, two threshold values, highlighted in underlined, italic, minimize their respective errors (below 30%, with the mean error however below 20%). These results have been obtained dividing the calibration interval into two ranges, as specified in Eqs. 9 and 10.

It is essential to specify, once again, that the choice of the number of ranges and their amplitude must tend to minimize

the maximum error in each chosen range.

$$\%\, err_D = \frac{D_{est} - D_{nom}}{D_{nom}} \times 100 \tag{6}$$

$$\%\, err_d = \frac{d_{est} - d_{nom}}{d_{nom}} \times 100 \tag{7}$$

$$\%\, err_{D/d} = \frac{(D/d)_{est} - (D/d)_{nom}}{(D/d)_{nom}} \times 100 \tag{8}$$

$$2 \leq \frac{D}{d} \leq 5 \quad Th_{D/d} = 0.6 \tag{9}$$

$$5 < \frac{D}{d} \leq 16 \quad Th_{D/d} = 0.4 \tag{10}$$

5.1.2 Demonstration of the Proposed Procedure on the Aluminium Specimen

In order to demonstrate the effectivness of the proposed procedure for the aluminium, the same test specimen is used, but considering the lower part of the specimen, where four unknown defects (red box in Fig. 4b) have been considered.

Three replications have been carried out keeping the test parameters and using the truncation window obtained as the final result in the calibration procedure (1.91 s).

In Fig. 9a is shown the EOF_2 map obtained after the PCT analysis of one replication. The *SBC* and also the related contrast C_{EOF_2} values have been assessed for each defect considering each replication.

In Fig. 9b are reported the contrast values, distinguishing the unknown defects with the cross symbol, and the defects used also in the calibration phase with an asterisk symbol. Entering the graph with the contrast value, it is possible to obtain the defect aspect ratio D/d value, applying the equation of the calibration curve, reported in Eq. 5.

The percentage values of errors in evaluating the defect size and depth are summarized in Table 2 and they have been obtained adopting the procedure illustrated in Table 1, distinguishing also, in this case, the defects used for the calibration procedure from the defects used for the demonstration (bold character). Error values lower than 10% have been highlighted with the symbol * while those greater than 20% with **.

As expected, the maximum errors have been obtained in depths evaluation and above all for low *D/d* values (see Table 2 for details) and therefore for the lowest values of the signal contrast. However, the mean error value in the estimation of depths is about 20% which can be considered quite satisfactory for engineering and non-destructive applications, and also for high diffusivity materials. Within the Table 2, the errors related to the aspect ratio estimation considering only the calibration curve, are also reported.

Moreover, it should be noted that the obtained errors are actually a sum of errors, systematics and random, due not only to the proposed procedure, but also to other noisy sources common to other literature methods, such as the thermal signal accuracy that depends on the used instrumentation, knowledge of the thermophysical parameters of materials, precision in test setup, the pulse duration and the used frame rate, the adopted geometrical resolution in terms of the mm/pixel ratio, etc. In future works, each error source will be considered in order to estimate the uncertainty in evaluating sizes and depths.

For completeness, the binarized maps obtained applying the proposed procedure are reported in Fig. 13, considering the two different threshold values highlighted in Eq. 6 (Fig. 13a) and 7 (Fig. 13b), with different colours and symbols for the defects used also for the calibration (light blue) and for the demonstration (green). In the two maps in Fig. 13, the defects for which that specific threshold has been chosen are generally coloured.

5.2 Results Related to the GFRP Specimen

5.2.1 Applying the Calibration Procedure to Investigate the GFRP Specimen

In this section, the results related to the calibration phase of the GFRP specimen are reported. It should be emphasized once again, that in this case, the analysis is referred to a completely different test and material, or a long impulse duration test (180 s), with halogen lamps and a cheaper thermal sensor.

The calibration procedure follows the same steps described before, analysing the entire thermal sequence after the mean subtraction. Again, the second component EOF_2 is the one that returns the greatest number of indications, then follows the analysis for searching the truncation window that provides the best correlation D/d-C_{EOF_2}, as shown in Fig. 14. The procedure to determine the most suitable truncation window size (analysis interval) is the same to the previous one described in the case of the aluminium specimen and reported as summary and result in Sect. 6.1.1. The procedure is independent of the acquisition frequency. The graph in Fig. 14 describes this choice, reporting the result of the various analyses in terms of R^2 and number of detected defects for each interval, expressed in seconds.

For the truncation window size of 36 s (36 frames of the cooling down, after 180 s of heating, map reported in Fig. 15a), the empirical correlation D/d-C_{EOF_2} results strongly linear (calibration curve reported in Fig. 15b). The number of detected defects is enough to obtain a realistic calibration curve with a good value of R^2 (8 defects, Fig. 14).

The next step consists of choosing the threshold values considering the defect aspect ratio *D/d* range. Also, in this

Table 1 Error analysis (percentage) for different threshold values (in Italic the $Th_{D/d}$ values chosen for the range indicated in Eqs. 8 and 9)

	$(D/d)_{nom}$	16.00	12.00	8.00	8.00	6.00	5.33	4.00	4.00	4.00	4.00	3.20	3.00	2.67	2.40	2.00	2.00
	D_{nom}	16.00	12.00	8.00	16.00	12.00	16.00	4.00	8.00	12.00	16.00	16.00	12.00	8.00	12.00	8.00	4.00
	d_{nom}	1.00	1.00	1.00	2.00	2.00	3.00	1.00	2.00	3.00	4.00	5.00	4.00	3.00	5.00	4.00	2.00
$Th_{D/d}$																	
0.30	$\%err_D$	0.32	0.61	15.80	25.01	31.67	27.02	98.20	175.66	35.23	19.07	50.10	21.40	67.33	52.77	54.26	133.71
	$\%err_d$	− 1.02	− 1.28	36.84	− 1.20	− 3.74	5.73	135.99	22.20	8.80	20.01	44.10	22.21	14.12	54.70	33.56	135.60
0.40	$\%err_D$	*− 6.74*	*− 5.66*	*14.59*	*− 4.05*	*− 4.38*	*− 4.24*	34.96	− 22.63	7.89	11.02	49.20	24.79	74.09	56.70	48.98	42.46
	$\%err_d$	*− 5.26*	*− 7.06*	*19.22*	*− 14.33*	*− 9.79*	*8.90*	51.29	− 24.70	20.89	22.68	46.45	30.44	55.26	53.73	49.49	47.35
0.50	$\%err_D$	− 14.47	− 14.48	− 4.29	− 11.77	− 12.13	− 12.20	26.77	− 24.57	− 0.68	− 4.05	35.12	8.03	41.63	31.56	37.56	37.53
	$\%err_d$	− 13.12	− 15.75	8.73	− 21.23	− 17.10	− 0.15	27.67	− 26.06	11.28	6.02	32.58	12.92	26.32	39.16	31.94	33.12
0.60	$\%err_D$	− 24.34	− 24.34	− 24.25	− 21.06	− 21.14	− 20.32	*17.67*	*− 18.88*	*− 11.47*	*− 17.31*	*21.56*	*− 2.53*	*18.18*	*25.08*	*24.19*	*24.22*
	$\%err_d$	− 23.14	− 25.46	− 2.36	− 29.52	− 25.61	− 9.40	*25.85*	*− 18.91*	*− 0.80*	*− 8.63*	*29.23*	*1.89*	*5.40*	*23.41*	*22.78*	*23.83*
0.70	$\%err_D$	− 39.01	− 37.32	− 33.23	− 42.03	− 35.00	− 12.90	− 12.87	− 26.16	− 34.84	− 16.69	− 15.91	− 26.13	− 31.32	− 17.75	− 22.89	3.79
	$\%err_d$	− 40.20	− 38.50	− 21.10	− 45.10	− 41.44	− 31.01	2.81	− 31.47	− 36.43	− 24.48	− 16.71	− 25.64	− 42.05	9.78	− 33.23	− 19.60

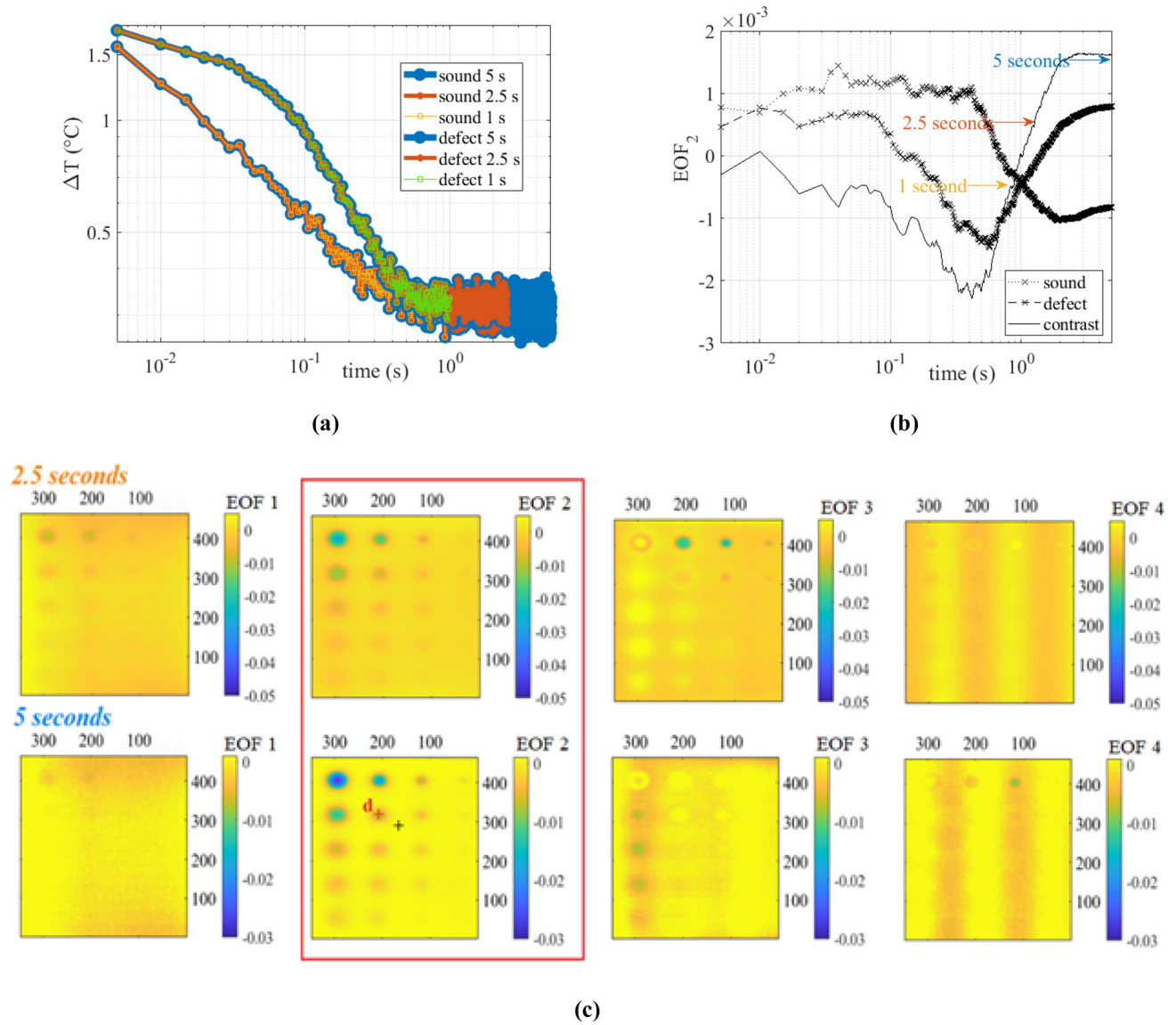

Fig. 8 Obtained results after the application of the PCT algorithm for different truncation windows (examples 2.5 and 5 s) and different EOFs (example 1st, 2nd, 3rd and 4th), (a) temporal trend of the thermal signal (example, diameter 12 mm, depth 2 mm), (b) temporal trend of the EOF_2 component (example, diameter 12 mm, depth 2 mm) and (c) EOFs images (with the indication of the defect taken as example)

case, the range of *D/d* is quite wide, and more than one threshold value needs to be used to obtain the smallest possible error in the chosen *D/d* range. For brevity, only the results in terms of relation *D/d-Th* are here reported:

$$\frac{D}{d} \leq 5 \quad Th = 0.6 \tag{11}$$

$$5 < \frac{D}{d} \leq 15 \quad Th = 0.5 \tag{12}$$

$$15 < \frac{D}{d} < 35 \quad Th = 0.4 \tag{13}$$

5.2.2 Validation of the Proposed Procedure on Real GFRP Component: A Real Case Study

The proposed analysis regards the study of a real component, that is a root of a wind turbine with large but very deep air gaps inside (depth of about 6 mm). The total area of the component under examination is 40 × 40 cm^2 with a variable thickness in a range of about 15–20 mm. In Fig. 16b the presence of one of these air gaps on one side of the component is highlighted. Again, the same test with a long pulse duration is performed, replicating the same setup and conditions of the GFRP sample with imposed defects.

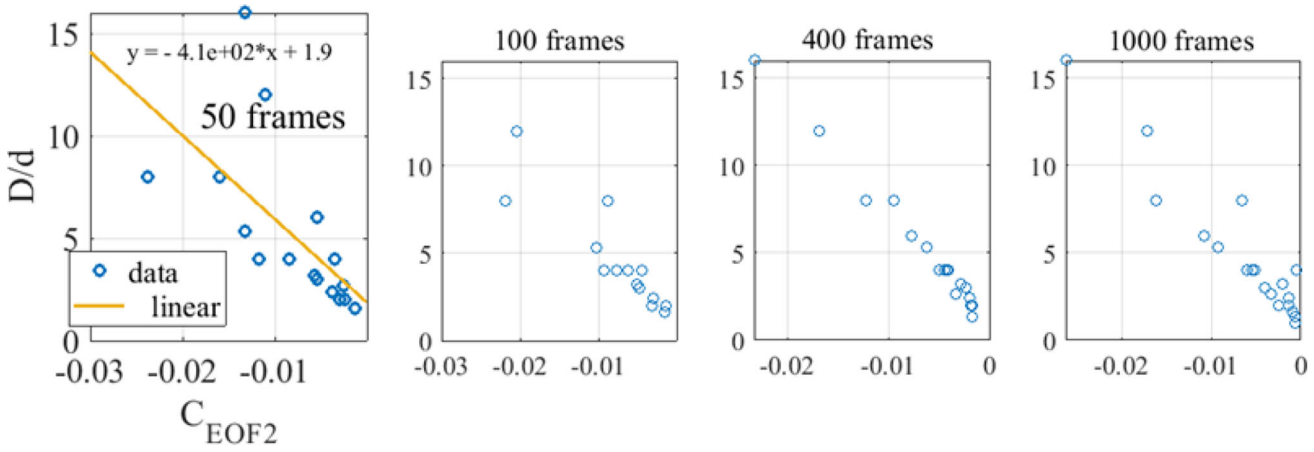

Fig. 9 Correlation between the signal contrast and the aspect ratios (D/d) of defects and its evolution for different truncation windows (number of frames)

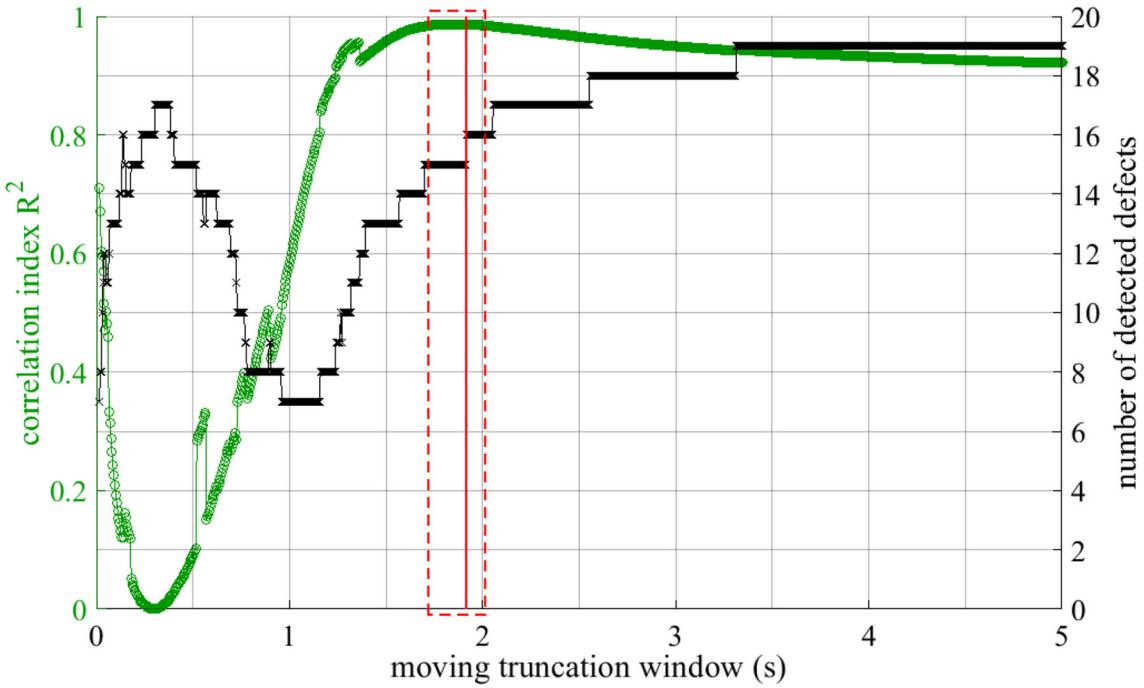

Fig. 10 Correlation index R^2 and detected defects obtained with the analysis on the EOF_2 component with different truncation windows—best interval 1.91–2 s

The typical thermal trends for the defect and the related undamaged area are shown in Fig. 17a, reporting as representative map a cooling frame (frame 360 of the entire sequence) corresponding to the time of 360 s Fig. 17b.

The results show the presence of 3 defects inside the real component (the indications are clear also during the heating, see thermal profiles in Fig. 17a).

For the post-processing analysis by means of PCT, only 36 s related to the cooling down have been used (236 s considering both heating and cooling phases), as prescribed by the analysis procedure carried out on the related GFRP standard specimen. The related EOF_2 map corresponding to this truncation window is reported in Fig. 18a.

A matrix of 5 × 5 pixels has been considered for both defect and undamaged area evaluation to obtain the signal contrasts for each defect, as indicated in Fig. 18b. The contrasts for each defect are reported later in Table 3 together with the defect aspect ratio values obtained considering the calibration curve.

To assess the in-plane size of defects with a real particular shape, the characteristic dimension or an equivalent diameter must be defined. As it is well known, real defects usually

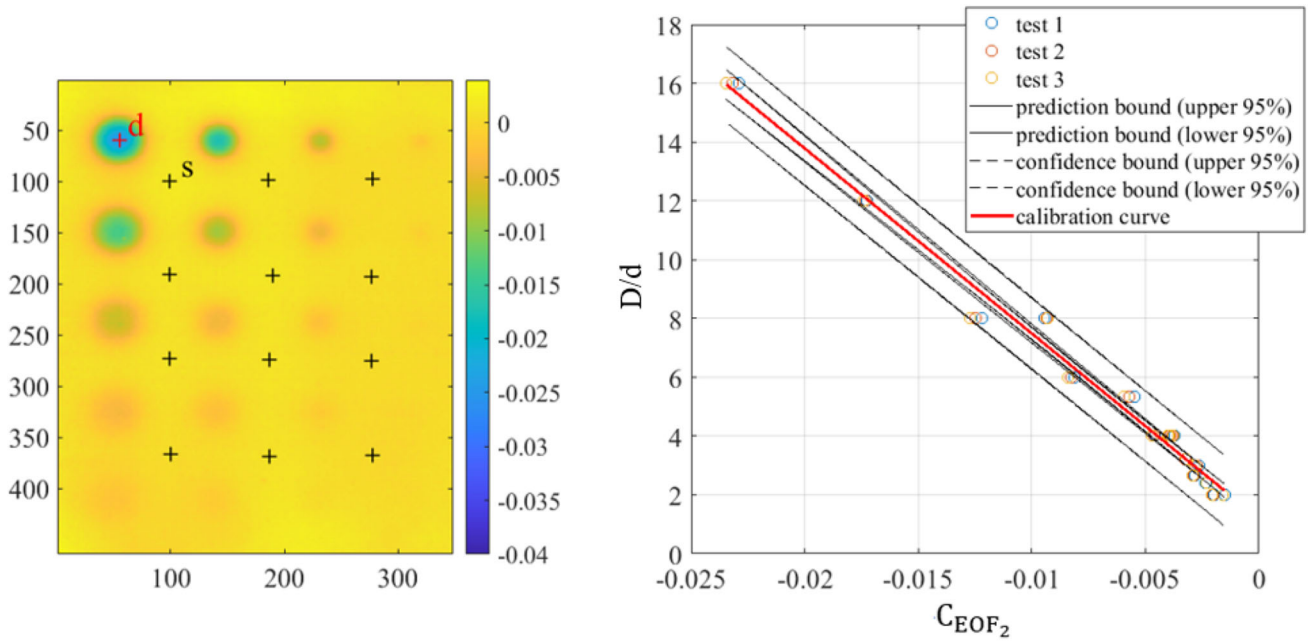

Fig. 11 (a) EOF_2 map obtained considering the truncation window of about 2 s and undamageds and defect area used to assess the signal contrast values, (b) calibration curve (3 repetitions)

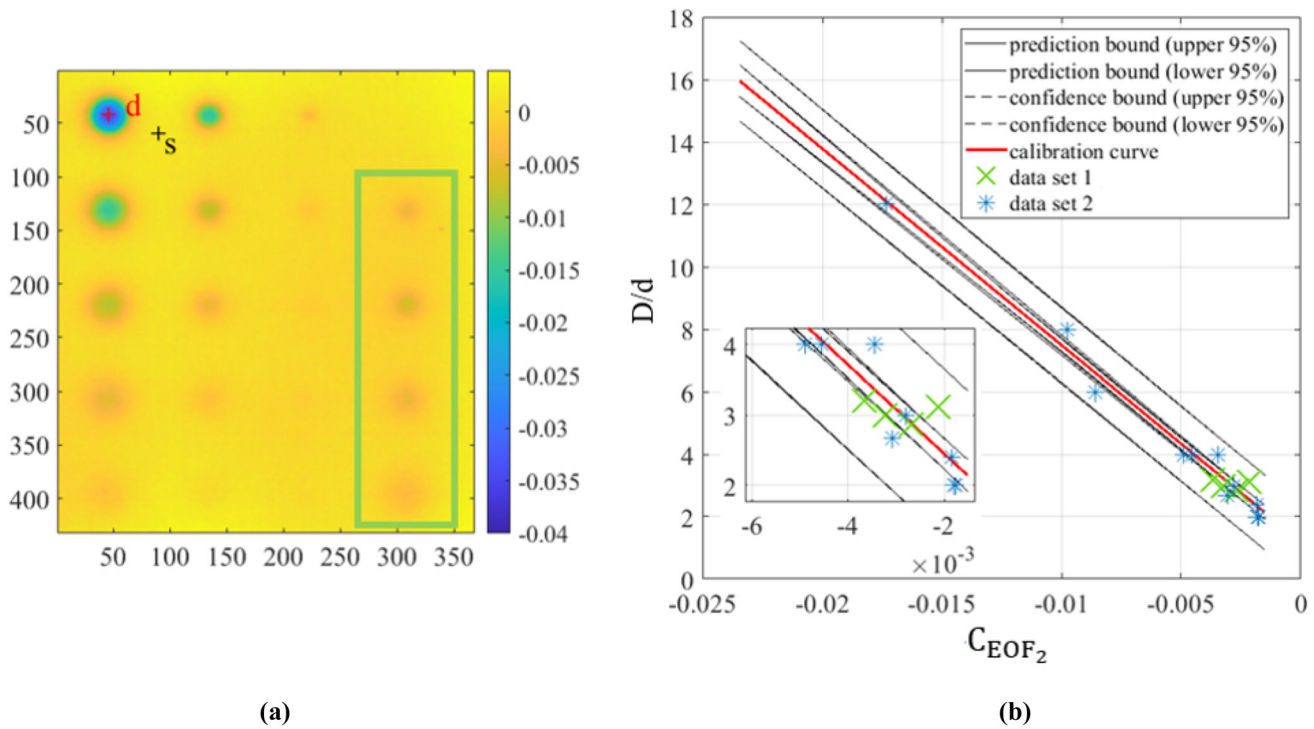

Fig. 12 (a) EOF_2 map referred to the chosen truncation window (2 s) and (b) position of the unknown defects indicated with green cross symbols within the calibration curve (data set 1) (Color figure online)

Table 2 Percentage errors related to this demonstration, when different threshold values are applied, based on the contrast values and the defect aspect ratios, according to the calibration phase Table 1

	$(D/d)_{max}$	12.00	8.00	4.00	6.00	4.00	2.00	3.00	4.00	2.67	3.20	3.00	2.00	2.86	2.4	3.11
	$\%err_{D/d}$	1.91	− 15.40	− 15.30	11.00	7.70	17.11	8.48	2.47	18.43	10.24	− 0.82	15.42	1.50	− 1.26	− 17.91
	D_{nom}	12.00	8.00	4.00	12.00	8.00	4.00	6.00	12.00	8.00	8.00	12.00	8.00	10.00	12.00	14.00
	d_{nom}	1.00			2.00				3.00		2.5	4.00		3.5	4.5	5.00
$Th_{D/d}$																
0.40	$\%err_D$	− 8.76*	1.90*		− 2.66*											
	$\%err_d$	− 10.48	20.42**		− 12.31											
0.60	$\%err_D$			4.33*		− 12.62	3.79*	5.54*	− 23.34**	− 13.82	0.01*	− 14.27	− 5.29*	− 1.78*	− 2.93*	6.61*
	$\%err_d$			23.10**		− 18.91	− 11.29	− 2.58*	− 25.21**	− 27.28**	− 9.34*	− 13.69	− 18.00	− 3.24*	− 1.70*	30.06**

*< 10%
**> 20%

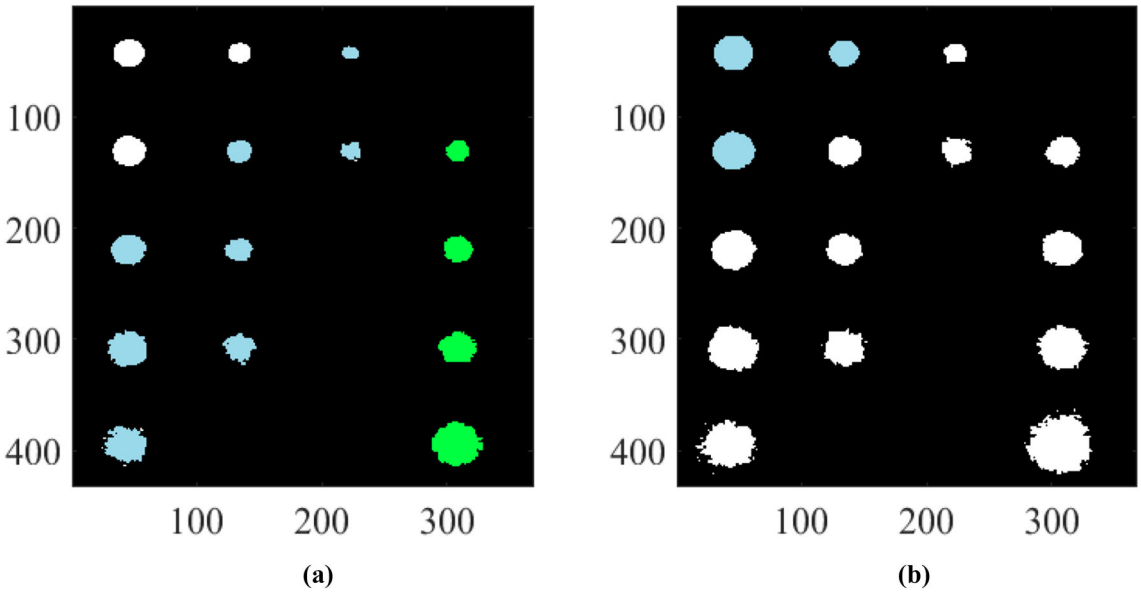

Fig. 13 Binarized maps corresponding to the lower part of the specimen used for the demonstration, when 2 different threshold values are applied based on the defect aspect ratio value (a) $Th_{D/d} = 0.6$ and (b) $Th_{D/d}$=0.4; in green the defects used and create only for the demonstration and in blue the defects used both for calibration and validation (Color figure online)

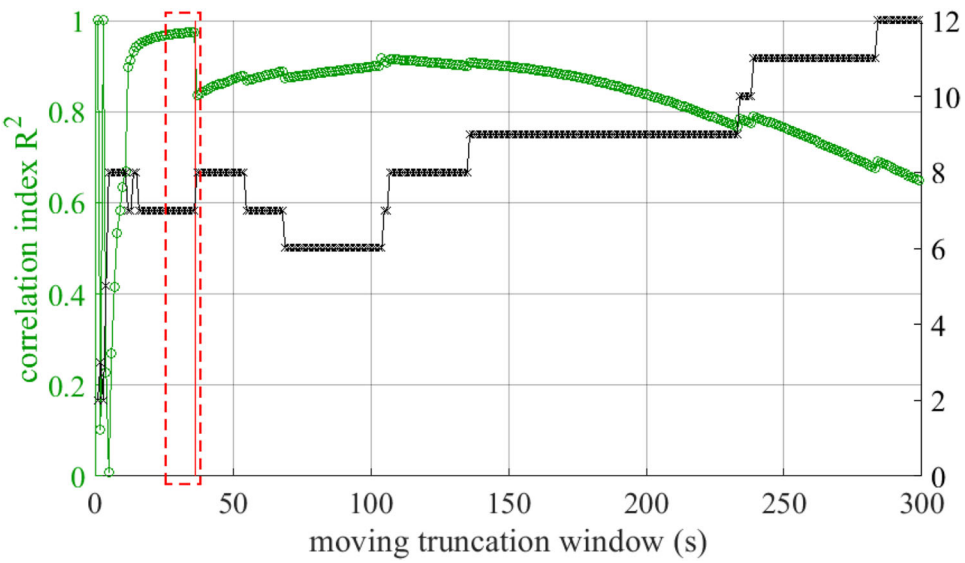

Fig. 14 Correlation index R^2 and detected defects obtained with the analysis on the EOF2 component with different truncation windows

present a non-regular in-plane shape that cannot be fitted with a regular geometric shape such as a circle or a square. Moreover, as already demonstrated in different previous works [19, 10–15, 20, 21], the signal contrast depends not only on the defect cross-section area, but also on its shape. So, to consider the influence of the defect shape on the signal contrast, a characteristic dimension, called in this work "equivalent diameter", has been considered representative of the in-plane defect size, using a general definition for which a generic ellipse, with major semi-axis 'a' and minor semi-axis 'b', is therefore a circle when 'a' and 'b' coincide, as reported in Eq. 14:

$$D = \sqrt{2\left(a^2 + b^2\right)\frac{b}{a}} \tag{14}$$

To find these typical dimensions in a defect with a particular shape the command *regionprops* in Matlab® has been used for the definition of the centroid for each defect and then the definition of the major and minor axis of the ellipse that includes the shape of the same.

In Fig. 19 are reported the binary maps obtained imposing the threshold values indicated in the Eqs. 8 and 9 and then,

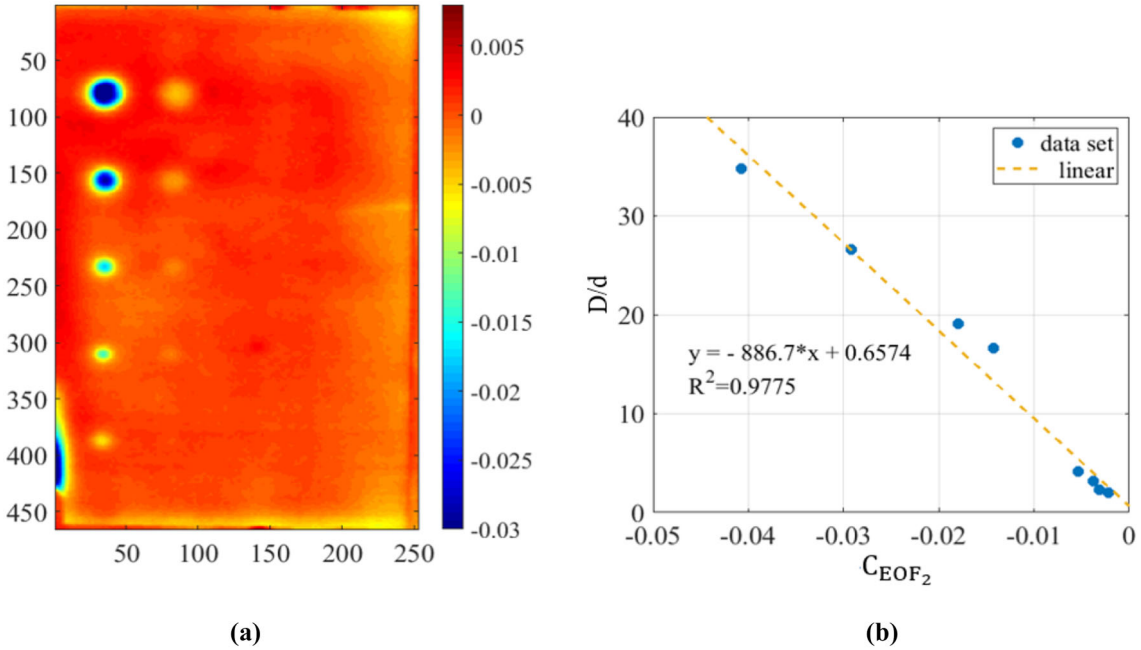

Fig. 15 (a) EOF_2 map referred to the chosen truncation window (36 s of analysis-cooling down) and (b) the related calibration curve

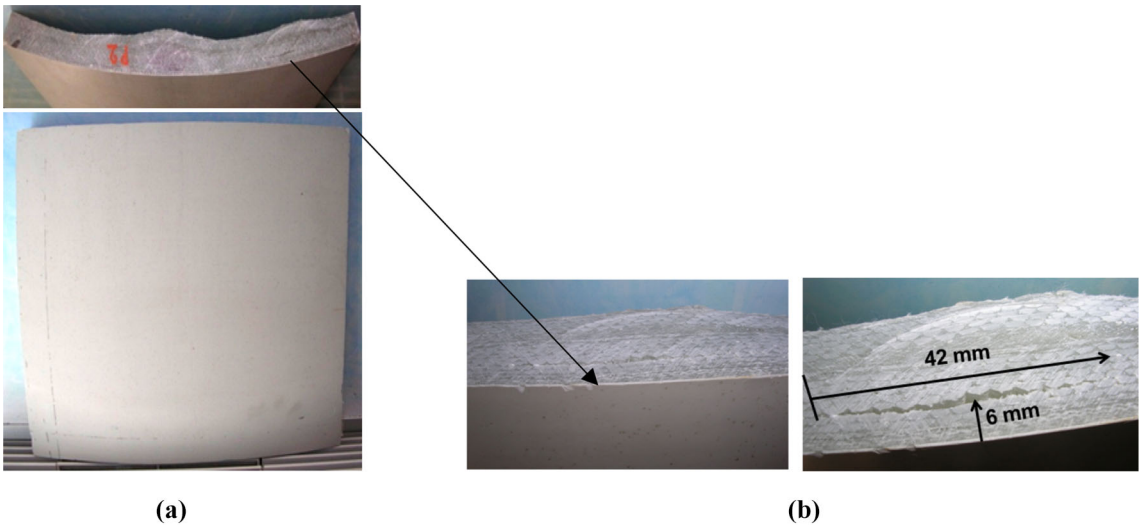

Fig. 16 (a) GFRP root of a wind blade and (b) particular of the defect with dimensions

in red, the indications of the two circles, one smaller and one larger, with centre the centroid and radii, respectively, the minor and major axis of the equivalent ellipse (in green).

To obtain the depth value, the characteristic dimension has been assessed as reported in Fig. 19b for the three considered defects, in blue, starting from the definition of the minor and major axes.

The depths of the three defects assessed with the proposed procedure have been compared with the ones obtained with the well-established UT technique. It is important to underline that the UT value has been obtained by placing the probe at the centre of the defect. The results, in Table 3, show that the proposed procedure allows for obtaining depth estimations in good agreement with the UT pulse-echo technique.

As already said, the GFRP sample shown before with flat bottom holes and so quasi-perfect reflectivity defects (the defect dimensions affect the reflection coefficient) has been used here for the validation on a real specimen with real defects. As the thermographic maps show in terms of contrast along the defect area—Fig. 18, the non-uniform thickness of the air gaps produces the variation within the same real defect of the signal contrast. Of course, to minimize errors in defects quantification, a perfectly correct training should be done

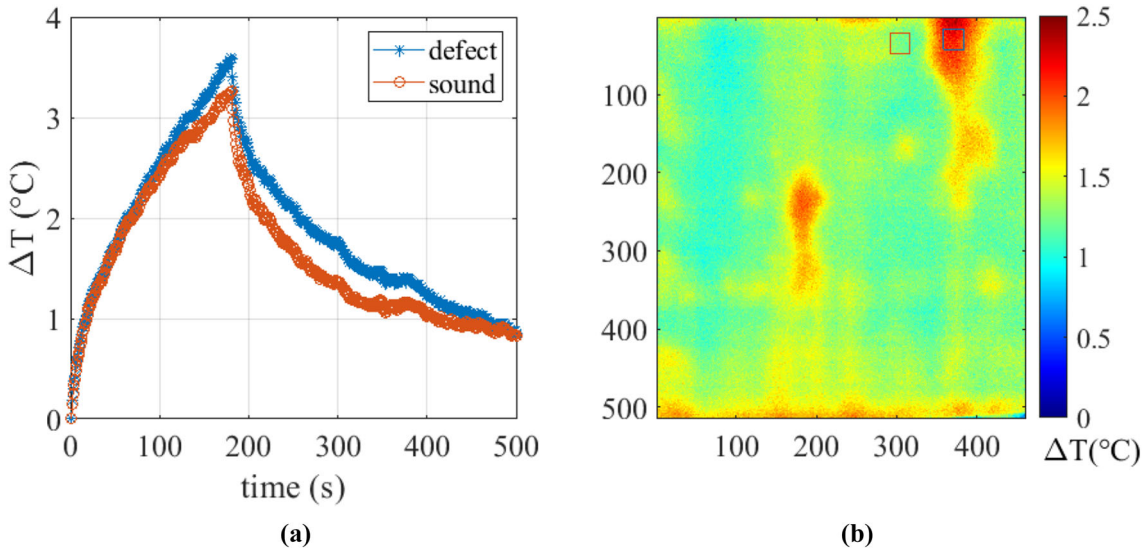

Fig. 17 (a) Thermal profiles related to the defected and undamaged areas, (b) frame 360 related to the cooling down

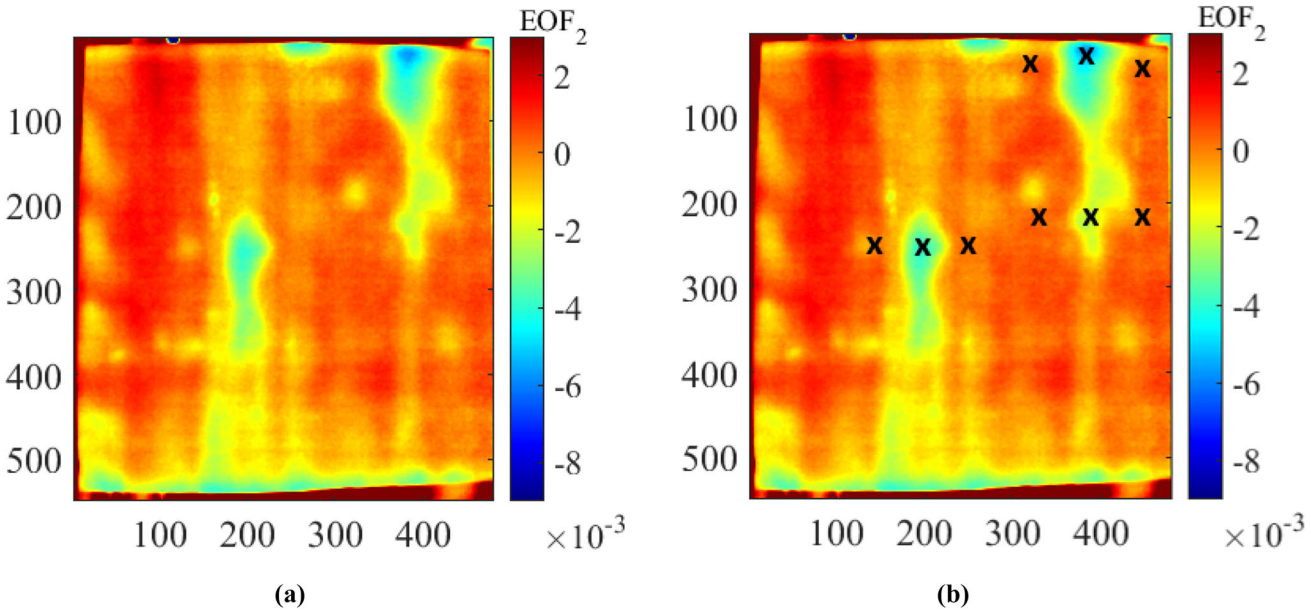

Fig. 18 Validation of the proposed procedure using the GFRP component: (a) map related to the EOF_2 component for a truncation window size of 36 s (cooling down) and (b) the same map with an indication of the areas used for assessing the signal contrast for each defect

considering for the calibration a sample specimen with simulated defects as close as possible to the real ones. However, in practical industrial applications regarding NDT techniques, it is difficult to produce a "perfect sample specimen", because is very hard to obtain the requested defects without increasing manufacturing costs (that can become unacceptable for industrial applications). On the other hand, it is worth to underline that, generally, also for other well-established NDT techniques such as Ultrasounds, the calibration curves are obtained by using flat bottom holes and then correcting them according to the real defect shape.

The good results obtained in our case are due to the high air gaps present in the GFRP component (above all at the centre of the defect in which the signal contrast has been considered) that is far from a close-contact delamination.

6 Conclusions

In this work, a new empirical procedure has been proposed to quantify defects in different materials applying the pulsed

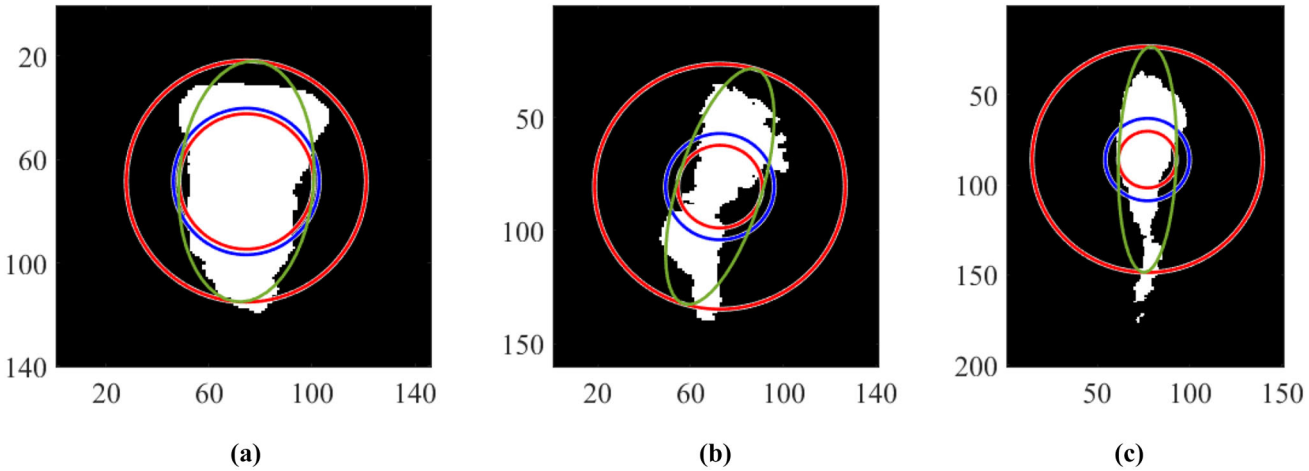

Fig. 19 Estimation of the equivalent diameter: (a) defect 1, (b) defect 2 and (c) defect 3

Table 3 Size and depth estimation of the three real defects and comparison with ultrasound results

	Contrast EOF_2	D/d	$Th_{D/d}$	Characteristic dimension D (mm)	Estimated depth d (mm) thermography	Estimated depth d (mm) ultrasound	% Err_d Thermography VS Ultrasound
Defect 1	− 0.0058	5.83	0.5	38.5	6.6	6.5	1.5
Defect 2	− 0.0024	2.76	0.6	31.9	11.6	12.1	− 4.1
Defect 3	− 0.0030	4.28	0.6	29.4	6.9	6.3	9.5

thermographic technique and then the PCT algorithm to very different setups.

The proposed procedure needs the design and manufacturing of a sample specimen with imposed defects of the same material as the real investigated component. In this regard, it is important to simulate a wide aspect ratio to cover the whole aspect ratio range expected in the real component. Furthermore, if the characteristics of the real defects are known, it is recommended to use a sample specimen with defects as similar as possible to the real. In this case, a correction factor for the shape, similar to the one proposed here, must be considered also during the calibration procedure.

The PCT has been used with a frame-by-frame analysis approach aimed to define the PCT component that returns the greatest number of indications and that, for a given truncation window, provides a strong linear correlation between the signal contrasts and defects aspect ratios.

Two different materials with very different thermal diffusivities have been investigated adopting two different setups: flash thermography for the aluminium and halogen lamps and the long pulse for the GFRP specimen. Moreover, the procedure has been validated on a GFRP real component with reals defects.

In the case of the aluminium specimen, the proposed procedure allows for estimating the size and the depth of the detected defects, with an average relative error of less than 20%. As expected, for the imposed defects, the highest errors have been obtained for deeper and smaller defects.

For the GFRP material, the results obtained with the proposed procedure on a real component with unknown defects have been compared by means of a consolidated technique such as the ultrasound one, with satisfactory results in estimating the depth of defects with an irregular shape. Furthermore, the influence of the shape factor has been evaluated. In this case, promising results were obtained considering the error committed in depth estimation was less than 10%. This result can be explained considering that the procedure was validated on air gaps defects, whose thermal behaviour can be considered like the simulated defects (FBHs), and different with respect to delaminations or other planar defects common in composite materials.

Finally, it is important to underline that the proposed procedure can be used also for long pulse tests, in which the hypotheses adopted by 1D models cannot be assured. This is the case of composite materials that require high heat energy to reach deeper defects, but, on the other hand, a lower frame rate and so the possibility to use low-cost IR sensors.

Future works will focus on the evaluation and influence of possible sources of error and on the measurement uncertainty.

Funding Open access funding provided by Politecnico di Bari within the CRUI-CARE Agreement.

References

1. Maldague, X.P.V.: Theory and practice of infrared technology of non-destructive testing. Wiley (2001). ISBN 0-471-18190-0
2. Oswald-Tranta, B.: Time and frequency behavior in TSR and PPT evaluation for flash thermography. QIRT J. **14**(2), 164–184 (2017)
3. Shepard, S.M., Lhota, J.R., Rubadeux, B.A., Wang, D., Ahmed, T.: Reconstruction and enhancement of active thermographic image sequences. Opt. Eng. **42**(5), 1337–1342 (2003)
4. Shepard, S.M., Hou, Y.L., Lhota, J.R., Golden, J.M.: Automated processing of thermographic derivatives for quality assurance. Opt. Eng. **46**(5), 510081–510086 (2007)
5. Balageas, D.L., Chapuis, B., Deban, G., Passilly, F.: Improvement of the detection of defects by pulse thermography thanks to the TSR approach in the case of a smart composite repair patch. In: 10th International Conference on Quantitative InfraRed Thermography (2010)
6. Ibarra-Castanedo, C.: Quantitative subsurface defect evaluation by pulsed phase thermography: depth retrieval with the phase, Collection Mémories et thèses électroniques (2005)
7. Ibarra-Castanedo, C., Maldague, X.: Pulsed phase thermography reviewed. Quant. InfraRed Thermography J. **1**(1), 47–70 (2004)
8. Marinetti, S., Plotnikov, Y.A., Winfree, W.P., Braggiotti, A.: Pulse Phase Thermography for Defect Detection and Visualization. Proc. SPIE **3586**, 230–238 (1999)
9. Rajic, N.: Principal component thermography for flaw contrast enhancement and flaw depth characterisation in composite structures. Compos. Struct. **58**(4), 521–528 (2002)
10. Sharath, D., Menaka, M., Venkatraman, B.: Effect of defect size on defect depth quantification in pulsed thermography. Meas. Sci. Technol. **24**(12), 25205 (2013)
11. Rothbart, N., Maierhofer, C., Goldammer, M., Hohlstein, F., Koch, J., Kryukov, I., et al.: Probability of detection analysis of round robin test results performed by flash thermography. Quant. InfraRed Thermogr. J. **14**(1), 1–23 (2017)
12. Zhao, Y., Mehnen, J., Sirikham, A., Roy, R.: A novel defect depth measurement method based on Nonlinear System Identification for pulsed thermographic inspection. Mech. Syst. Sig Process. **85**, 382–395 (2017)
13. Maierhofer, C., Röllig, M., Gower, M., Lodeiro, M., Baker, G., Monte, C., et al.: Evaluation of different techniques of active thermography for quantification of artificial defects in fiber-reinforced composites using thermal and phase contrast data analysis. Int. J. Thermophys. **39**(5), 61 (2018)
14. D'Accardi, E., Palumbo, D., Tamborrino, R., Galietti, U.: A Quantitative Comparison among Different Algorithms for Defects Detection on Aluminum with the Pulsed Thermography Technique. Metals **8**(10), 859 (2018)
15. D'Accardi, E., Palumbo, D., Tamborrino, R., Galietti, U.: (2019) The influence of the truncation window size on the quantitative thermographic results after a pulsed test on an aluminium sample: comparison among different post-processing algorithms. Proc. SPIE 11004, 110040 M. doi: https://doi.org/10.1117/12.2518984
16. Tomic, L.D., et al.: Application of Pulsed Flash Thermography Method for Specific Defect Estimation in Aluminum. Therm. Sci. **19**(5), 1845–1854 (2015)
17. Ibarra-Castanedo, C., Maldague, X.P.: Defect depth retrieval from pulsed phase thermographic data on plexiglas and aluminum samples. Thermosense XXVI International Society for Optics and Photonics **5405**, 348–357 (2004)
18. Zhi, Z., Ning, T., Lichun, F., Cunlin, Z.: Specified value based defect depth prediction using pulsed thermography. J. Appl. Phys. Report no. 2, p. 023112 (2012)
19. Vavilov, V.P., Burleigh, D.D.: Review of pulsed thermal NDT: physical principles, theory and data processing. NDT & E International **73**, 28–52 (2015)
20. Müller, J.P., Dell'Avvocato, G., Krankenhagen, R.: Assessing overload-induced delaminations in glass fiber reinforced polymers by its geometry and thermal resistance. NDT & E (2020) International 102309
21. Chulkov, AO, Sommier, A., Pradere, C., Vavilov, V.P., Siddiqui, A.O., Prasad, Y.L.V.D.: Analyzing efficiency of optical and THz infrared thermography in nondestructive testing of GFRPs by using the Tanimoto criterion. NDT & E International **117**, 102383 (2020)
22. Almond, D.P., Pickering, S.G.: An analytical study of the pulsed thermography defect detection limit. J. Appl. Phys. **111**, 093510 (2012)
23. Almond, D.P., Angioni, S.L., Pickering, S.G.: Long pulse excitation thermographic non-destructive evaluation. NDT & E International **87**, 7–14 (2017)
24. Lugin, S., Netzelmann, U.: A defect shape reconstruction algorithm for pulsed thermography. NDT & E International **40**(3), 220–228 (2007)
25. Wysocka-Fotek, O., Maj, M., Oliferuk, W.: Use of pulsed IR thermography for determination of size and depth of subsurface defect taking into account the shape of its cross-section area, 60. Archiv. Metall. Mater. (2015)
26. D'Accardi, E., Altenburg, S., Maierhofer, C., Palumbo, D., Galietti, U.: Detection of typical metal additive manufacturing defects by the application of thermographic techniques. In: Multidisciplinary Digital Publishing Institute Proceedings, vol. 27, pp. 1–24 (2019)
27. Feuillet, V., Ibos, L., Fois, M., Dumoulin, J., Candau, Y.: Defect detection and characterization in composite materials using square pulse thermography coupled with singular value decomposition analysis and thermal quadrupole modeling. NDT & E International **51**, 58–67 (2012)
28. Omar, M.A., Parvataneni, R., Zhou, Y.: A combined approach of selfreferencing and Principal Component Thermography for transient, steady, and selective heating scenarios. Infrared Phys. Technol. **53**(5), 358–362 (2012)
29. Yousefi, B., Sfarra, S., Castanedo, C.I., Maldague, X.P.: Thermal ndt applying candid covariance-free incremental principal component thermography (ccipct). In: Thermosense XXXIX International Society for Optics and Photonics p. 102141I (2017)
30. Wu, J.Y., Sfarra, S., Yao, Y.: Sparse principal component thermography for subsurface defect detection in composite products. IEEE Trans. Industr. Inf. **14**(12), 5594–5600 (2018)

31. D'Accardi, E., Palano, F., Tamborrino, R., Palumbo, D., Tatì, A., Terzi, R., Galietti, U.: Pulsed phase thermography approach for the characterization of delaminations in cfrp and comparison to phased array ultrasonic testing. J. Nondestr. Eval. **38**(1), 20 (2019)
32. Généreux, L.A., Viens, M., Lebrun, G.: Comparison of ultrasonic testing and infrared thermography for the detection of machining defects in composite materials (2011)
33. Quattrocchi, A., Freni, F., Montanini, R.: Comparison between air-coupled ultrasonic testing and active thermography for defect identification in composite materials. Nondestruct. Test. Eval. (2019). https://doi.org/10.1080/10589759.2019.1699084
34. Maierhofer, C., Krankenhagen, R., Röllig, M., Heckel, T., Brackrock, D., Gaal, M.: Quantification of impact damages in CFRP and GFRP structures with thermography and ultrasonics. QIRT-2018-126 (2018)
35. Roche, J.M., Balageas, D.L.: Common tools for quantitative pulse and step-heating thermography—Part II: Experimental investigation. Quant. InfraRed Thermogr J. **12**, 1–23 (2015)
36. Meola, C.: A new approach for estimation of defects detection with infrared thermography. Mater. Lett. **61**(3), 747–750 (2007)
37. Palumbo, D., Cavallo, P., Galietti, U.: An investigation of the stepped thermography technique for defects evaluation in GFRP materials. NDT&E Int. **102**, 254–263 (2019)
38. Balageas, D.L., Roche, J.M.: Common tools for quantitative time-resolved pulse and step-heating thermography - Part I: Theoretical basis. Quant. InfraRed Thermogr J. **11**, 43–56 (2014)

39. JCGM 100:2008 (E). Guide to the expression of uncertainty in measurement
40. Montgomery, D.C., Runger, G.C.: Applied Statistics and Probability for Engineers, 5th edn. Wiley, New York (2011)